

# The BMW Detection Algorithm applied to the Chandra Deep Field south: deeper and deeper

A. Moretti<sup>1</sup>, D. Lazzati<sup>2</sup>, S. Campana<sup>1</sup>, G. Tagliaferri<sup>1</sup>

`moretti@merate.mi.astro.it`

## ABSTRACT

Chandra deep fields represent the deepest look at the X-ray sky. We analyzed the Chandra Deep Field South (CDFS) with the aid of a dedicated wavelet-based algorithm. Here we present a detailed description of the procedures used to analyze this field, tested and verified by means of extensive simulations. We show that we can safely reconstruct the Log N–Log S source distribution of the CDFS down to limiting fluxes of  $2.4 \times 10^{-17}$  and  $2.1 \times 10^{-16}$  erg s<sup>-1</sup> cm<sup>-2</sup> in the soft (0.5–2 keV) and hard (2–10 keV) bands, respectively, fainter by a factor  $\gtrsim 2$  than current estimates. At these levels we can account for  $\gtrsim 90\%$  of the 1–2 keV and 2–10 keV X-ray background.

*Subject headings:* X-ray background – number-counts – detection algorithm

## 1. Introduction

The Chandra observatory is providing the astronomical community with the deepest X-ray look at the sky (Mushotzky et al. 2000; Hornschemeier et al. 2000; Giacconi et al. 2001). Two 1 Ms observations have been recently carried out: one in the northern hemisphere on the Hubble Deep Field North (HDFN) and the other in the southern hemisphere on a field, named Chandra Deep Field South (CDFS), selected for its low column density (the southern twin of the Lockman hole) and for the lack of bright X-ray and optical sources. The data are available from the Chandra public archive

(<http://asc.harvard.edu/udocs/ao2-cdf-download.html>) A further 1 Ms data set on the HDFN will be available in the next future.

---

<sup>1</sup>Osservatorio Astronomico di Brera, Via E. Bianchi 46, Merate (LC), 23807, Italy.

<sup>2</sup>Institute of Astronomy, University of Cambridge, Madingley Road, Cambridge CB3 0HA, UK.

The main goal of these observations is to look at the X-ray sky at the deepest level and to gain insight in the population of emitting sources comprising the cosmic X-ray background (XRB). The details of the data reduction and analysis procedures that have been applied to manage the CDFS data-set are discussed in Section 2. In order to fully exploit the potential of these data, refined detection algorithm have to be used. We developed a wavelet-based source detection algorithm (Lazzati et al. 1999; for its main characteristics see also Section 3), that we applied to the full sample of ROSAT HRI fields (Campana et al. 1999; Panzera et al. 2002, in preparation). We modified this detection algorithm, called Brera Multi-scale Wavelet (BMW), to account for the specific characteristics of the Chandra ACIS Imaging and Spectroscopic instruments. The algorithm (BMW-Chandra) has been extensively tested in the extreme conditions provided by the CDFS (Section 4). Our final goal is to obtain a source detection and a source Log N–Log S at the faintest limits in order to resolve as much as possible of the XRB in point sources. In order to compare our results with previous investigations, we carry out the analysis in the soft (0.5–2 keV) band and in the hard (2–10 keV) band. We are able to safely reconstruct the Log N–Log S source flux distribution down to  $2.4 \times 10^{-17}$  and  $2.1 \times 10^{-16}$  erg s<sup>-1</sup> cm<sup>-2</sup> in the soft and hard bands, respectively (Section 5). A first account of these results have been given in Campana et al. (2001), here we extend these results discussing in more details the resolved background and source characteristics. Conclusions are reported in Section 6.

## 2. The data

All exposures were taken with the Chandra X-ray Observatory (Weisskopf et al. 2000) Advanced CCD Imaging Spectrometer (ACIS-I) detector (Bautz et al. 1998). ACIS-I consists of four CCDs arranged in a  $2 \times 2$  array assembled in an inverse shallow pyramid configuration to better follow the curved focal surface of the mirrors. The full ACIS-I has a field of view of  $16.9' \times 16.9'$ . The on-axis image quality is  $\sim 0.5''$  FWHM increasing to  $\sim 3.0''$  FWHM at  $\sim 4.0'$  off-axis. The CDFS has been obtained performing eleven exposures of the same area of the sky with slight position and orientation offsets. A total exposure time of 966 ks is obtained by summing them together. In Tab. 1 we report the main properties of each exposure.

First we have to match the position of the different exposures to add them into a single image. To this aim we performed a preliminary source detection on the 11 sub-frames at full resolution. We used the grid of the positions of the brightest sources to calculate the ten roto–translation matrices with respect to the first image. In all ten matrices we find that the rotation terms are negligible. The translation factors of each frame with their uncertainties

are reported in Tab. 1. The reported uncertainties are the standard deviations of the position distributions of the grid sources after the translations.

Starting with the level 2 event files, the data were filtered to include only the standard event grades (corresponding to the ASCA grades 0, 2, 3, 4, 6). In order to compare our results with previous studies and existing estimates of the cosmic X-ray background, we selected a 0.5–2 keV soft energy band and a 2–7 keV hard energy band to carry out the scientific analysis. The limit at 7 keV has been selected because at higher energies the effective area decreases and the background increases, resulting in a lower signal to noise of celestial sources. The fluxes are then extrapolated to the 2–10 keV energy band.

Chandra observations are affected by the ‘space weather’, resulting in periods with high background. In order to eliminate these periods we calculated the total counts light curve for each exposure using a time resolution such that in each bin we had  $\sim 400$  events (i.e.  $\sim 1,000$  s in the soft band and  $\sim 600$  s in the hard band). We excluded all time intervals above  $3\sigma$  of the mean. From a total of 966 ks, we excluded 24 ks in the soft band (28 ks in the hard band), giving a final effective exposure time of 942 ks (939 ks in the hard). The lost fractions amount to  $\sim 3\%$  of the total time, but allowed us to reduce considerably the background in each band. In particular, we registered a very strong flare in the observation ID1431 which contained about 90% of the total events both in the soft and hard band in about 10% of the exposure time.

CCDs are usually affected by defects such as bad columns, bad and hot/flickering pixels and cosmic ray events. The great majority of these defects are already eliminated by the standard Chandra processing pipeline. Random flickering pixels (probably excited by energetic cosmic rays) however do occur and have to be removed manually. These are active pixels for only 2–6 frames and might be easily detected as X-ray sources. Following Tozzi et al. (2001), we defined a pixel as “flickering” when it registers two events within the time of two consecutive frames and in each observation we eliminated all the events registered from that pixel (this can be done safely thanks to the lack of bright sources). In this way we excluded about 600 events in the soft band whereas in the hard band we did not find any flickering pixels. We also eliminated the data from chip 3 of the ID581 observation, because it suffered from Good Time Intervals inconsistencies with other chips, resulting in an anomalous high background level.

The count-rate to flux conversion factors in the 0.5–2 keV and in the 2–10 keV bands were taken from Tozzi et al. (2001). These were computed using the response matrices at the aim point and amount to  $(4.6 \pm 0.1) \times 10^{-12}$  erg s $^{-1}$  cm $^{-2}$  per count s $^{-1}$  (0.5–2 keV), and  $(2.9 \pm 0.3) \times 10^{-11}$  erg s $^{-1}$  cm $^{-2}$  (2–10 keV) per count s $^{-1}$  in the hard band, assuming a Galactic absorbing column of  $8 \times 10^{19}$  cm $^{-2}$  and a photon index  $\Gamma = 1.4$ , i.e.

the spectrum of the XRB. Flux uncertainties are derived considering power law indices in the range  $\Gamma = 1.1 - 1.7$ . Fluxes are corrected for vignetting by using the exposure map (see below).

The analysis has been carried out on images rebinned by a factor of 2 (i.e. 1 pixel corresponds to 0.98 arcsec), allowing us to deal directly with the entire image. We found that working on sub-images at the natural scale improves slightly the positional accuracy at the price of a four times longer computational time and with the problem of matching the four sub-images.

In the analysis of the CDFS we have restricted our analysis to the central 8 arcmin radius circle, assuming as the center the aim point of ID581 observation. This is a good compromise between the simplicity of the geometry and the efficiency of the data analysis (see below). The minimum value of the exposure map in this region is about 23% of the maximum value. This occurs at the border of the circle where the exposure map has a very steep decrease. More than 90% of the exposure map within the 8 arcmin central circle have values larger than 80% of the maximum value, corresponding to an effective exposure time greater than 753 ks. The average background levels in this region are 0.18 and 0.29 counts per binned pixel in the soft and hard band, respectively. These correspond to 0.07 and 0.11 counts  $s^{-1}$  per chip and are in very good agreement with the expected value reported in the Chandra Observatory Guide.

### 3. The BMW algorithm

The wavelet transform (WT) is a mathematical tool able of decomposing an image in a set of sub-images, each of them carrying the information of the original image at a given scale. These features make the WT well suited for the analysis of X-ray images, where the scale of sources is not constant over the field of view. In addition, the background is automatically subtracted since it is not characterized by any scale. The use of WT as X-ray detection algorithms was pioneered by Rosati et al. (1995; 1998) for the detection of extended sources in ROSAT PSPC fields and subsequently adopted by many groups (Grebenev et al. 1995; Damiani et al. 1997a; Pislar et al. 1997; Vikhlinin et al. 1998; Lazzati et al. 1998; Freeman et al. 2001).

The BMW detection algorithm is a WT-based algorithm for the automatic detection and characterization of sources in X-ray images. It is fully described in Lazzati et al. (1999) and has been developed to analyze ROSAT HRI images producing the BMW-HRI catalog (Campana et al. 1999; Panzera et al. 2002). We have recently updated this algorithm to

support the analysis of Chandra ACIS Imaging and Spectroscopic images. Here we summarize the basic steps of the algorithm. First, the WT of the input image is performed. The BMW WT computation is based on the discrete multi-resolution theory and on the “á trous” algorithm (Bijaoui et al. 1991). This is different with respect to algorithms based on a continuous WT, which can sample more scales at the cost of longer computing time (Rosati et al. 1995; Grebenev et al. 1995; Damiani et al. 1997a). We used a Mexican hat mother, which can be analytically approximated by the difference of two Gaussians (Slezak et al. 1994). We performed the Chandra ACIS-I data analysis with a rebin factor of 2 and we used the scales  $a = 1, 2, 4, 8, 16$  and 32 pixels, where  $a$  is the scale of the transform (see Lazzati et al. 1999).

Candidate sources are identified as local maxima above the threshold in the wavelet space at each scale. A catalog for each scale is obtained. Different scale catalogs are then cross-correlated and merged in a single catalog. For each scale the threshold in the wavelet space is calculated by means of Monte Carlo simulations: for a grid of values of Poissonian backgrounds in the range between  $10^{-4} - 10^1$  counts per pixel we estimated the number of expected spurious detections as a function of the threshold value. The background value is measured as an average on the whole image by means of a  $\sigma$ -clipping algorithm. The number of spurious sources per field can be fixed arbitrarily by the user (typical values are in the range 0.1 – 10). At the end of this detection step we have a first estimate of the source position, an estimate of the counts from the local maximum value of the WT and a guess of the size from the scale where the WT is maximized.

The final catalog is obtained through the characterization of the sources, which is performed by means of a  $\chi^2$  minimization with respect to a Gaussian model source in the wavelet space. The WT of a detected source is used at three different scales, with the central being the scale at which the source has been found (corrections are introduced when the best scale is the first or the last). In order to fit the model on a set of independent data, the WT coefficients are decimated according to the scheme described in Lazzati et al. (1999). Neighbor sources can be fitted simultaneously in the deblending process, allowing the characterization of faint objects located near bright sources.

### 3.1. Total background map

The WT detection is carried out on top of a map representing at best the image background (named total background map, see Lazzati et al. 1999). The ACIS-I background consists of two different components, the cosmic X-ray background and cosmic ray-induced events (also called particle background). The first is made by focalized X-ray photons

from not resolved sources and therefore suffers from mirror vignetting. Its spectrum can be modelled as a power law with photon index  $\Gamma = 1.4$ . Following the CIAO 2.1 Science Threads (<http://asc.harvard.edu/ciao/threads>) we built the exposure maps for each of the eleven observations (both in the soft and in the hard band) assuming a photon index  $\Gamma = 1.4$  as input spectrum. The second contribution has a spatial pattern which is basically due to the electronics of the system and depends on its temperature. Based on the Chandra ACIS background web page

([http://asc.harvard.edu/cal/Links/Acis/acis/Cal\\_prods/bkgrnd/current/index.html](http://asc.harvard.edu/cal/Links/Acis/acis/Cal_prods/bkgrnd/current/index.html)) we found that for the ACIS-I chips in the energy range and in the spatial region of interest for the only particle background we can assume a spatial flat pattern with an inaccuracy of less than 10%. We assumed that the particle background in the soft band is 50% of the total and the 66% in the hard band with a flat energy spectrum (Baganoff 1999). Summing the two components of the background we obtain a total background map and taking a Poissonian realization of it we can accurately account for the data in both bands as shown in Fig. 1. This procedure is slightly different from the one adopted in Campana et al. (2001), where a map based only on the cosmic X-ray background was considered.

#### 4. Simulations

We tested the detection algorithm, trying to reproduce the real data in terms of background level and source flux distribution, matching the characteristics of the CDFS fields. The analysis is carried out in two energy bands: the soft (0.5–2 keV) and the hard (2–7 keV) band. From the detection algorithm point of view the two bands differ for two main reasons: the shape of the exposure maps and the different background level. This forced us to carry out two different sets of simulations.

X-ray sources were generated at random positions in a  $30' \times 30'$  square region around the center of the image (larger than the real field of view) and with fluxes distributed in the range  $10^{-17} - 10^{-13}$  erg s $^{-1}$  cm $^{-2}$  for the soft band and  $10^{-16} - 10^{-13}$  erg s $^{-1}$  cm $^{-2}$  in the hard band. The number counts have been generated according to the Log N–Log S integral distributions reported in Tozzi et al. (2001), i.e. power laws with slope of 0.66 in the soft band and 0.92 in the hard band.

The CDFS is made of eleven observations. For this reason we added a further element to our simulations: for each source we calculated its position in each observation and derived the corresponding off-axis angle (each source has different positions in the detector in each different observation, depending on the coordinate of the pointing, which are slightly different, and on the roll angle). Then we calculated the expected number of photons for each

observation. These depend on the conversion factor and on the local value of the exposure map. Finally, for each single observation we multiplied the expected number of photons with the corresponding point spread function image (from the Chandra CALDB) and we summed the eleven images to the background image. This procedure is aimed at reproducing at best the image characteristics.

We used these routines instead of the MARX simulator essentially because of computational reasons: we found that dealing with the input/output of data was easier for us using our IDL routines. We repeated the procedure for 100 times, for a total sample of about 150,000 input sources (here and in the following we refer to simulations in the soft band, unless otherwise stated; in the hard band results are similar). We recovered 25,000 of them within the central 8 arcmin radius, from which we were able to verify the performance of the procedure.

#### 4.1. Spurious detection and position determination

In the BMW detection algorithm the expected number of spurious sources is one of the fundamental input parameters. In our analysis we fixed the number of spurious sources to a total of 4.3 in the 8 arcmin radius circle (which corresponds to 6 expected spurious in a  $1024 \times 1024$  pixels image). In 100 simulated frames we found a total of 425 spurious sources (431 expected, see left panel of Fig. 2). This shows that the contamination of our sample is well understood and under control. This corresponds to sources detected at a significance level larger than  $4\sigma$ .

Source positions are recovered accurately. In the right panel of Fig. 2 we plot the differences between the input and output position of simulated sources. The difference distributions on both axes are well approximated by Gaussian functions centered on zero and with a r.m.s. of  $0.6''$  (i.e.  $\sim$  half a pixel at rebin 2, at which the analysis has been carried out).

#### 4.2. Sky-coverage

The distribution of the detected sources is usually depleted at the faint end. In order to compute the Log N–Log S it must be corrected for (i) detection probability lower than one close to the sensitivity limit (completeness function; CF) and (ii) the different areas effectively surveyed at different fluxes (sky coverage; SC). The CF is due to the fact that sources are preferentially detected if they sit on a positive background fluctuation, while

they are missed in the opposite case. The proper SC takes into account that the sensitivity limit can change in the same observation if the background or spatial resolution are not uniform or in different observations when different exposure times are considered. In single observations the SC depends on the off-axis angle, since the detector sensitivity decreases (lower effective exposure time) and the spatial resolution worsen. In the CDFS the geometry is complicated by the sum of observations with slightly different aim points and different roll angles. We have verified that this fact does not affect significantly the symmetry of the SC. More importantly, the SC has strong variations in those locations of the sky that were not imaged in all the eleven observations. In order to avoid large SC fluctuations, we restricted our analysis to the inner  $8'$  of the field, where the background and exposure are roughly constant (see above).

Using WT based detection algorithms the SC can be computed either analytically or by means of simulations. The first approach is recommended when the intrinsic size of sources is poorly known (like in surveys of cluster of galaxies, see Rosati et al. 1995). In the CDFS the presence of extended sources is a minor effect for the computation of the Log N–Log S. For this reason we computed the SC by comparing the input and output number counts of simulated fields. We divided the selected field of view into four circular regions ( $0' - 3'$ ,  $3' - 5'$ ,  $5' - 6.5'$  and  $6.5' - 8'$ ) and derived the SC and CF from simulations as a single correction (which we hereafter will call sky coverage). In the upper panels of Fig. 3 the derived CF as a function of flux and off-axis angle is shown for the soft and hard band; in the lower panels the total sky-coverages are shown in unit of square degrees.

### 4.3. Fluxes and bias correction

In Fig. 4 we show the comparison between the input and output counts of simulated sources (output fluxes are corrected for the flux lost during the WT characterization, i.e. the so-called Point Spread Function (PSF) correction, evaluated on bright isolated sources for every arcmin of the field of view, and vignetting, evaluated directly from the exposure map). For high signal to noise sources the counts are measured correctly, while at lower signal to noise ratio the count distribution of the detected sources suffers from the well known Eddington bias (e.g. Hasinger et al. 1993). In our case the bias starts affecting the data below  $\sim 30$  input counts in the soft band (corresponding to  $\sim 10^{-16}$  erg s $^{-1}$  cm $^{-2}$ ). This bias is due to the superposition of faint sources (below the detection threshold) on positive background fluctuations, making them detectable. Given the background level we expect to detect sources with less than 10 counts only in correspondence of background peaks (or when two faint sources are merged together into a brighter one). It follows that the counts of

the very faint sources are necessarily overestimated (otherwise they could not be detected). We corrected for this bias following the approach of Vikhlinin et al. (1995). We fitted the output source counts as a function of the input counts with polynomial functions for a grid of circular coronae, since the bias is a function of the source width (see Fig. 4). By inverting the fitting functions, we get an unbiased estimate of the source counts in the faint tail of the simulated sample. Input counts versus corrected output counts are shown in the right panel of Fig. 4.

To assess the goodness of our correction procedure we perform a maximum likelihood fit to the differential (unbinned) flux distributions of the 100 simulated fields individually and we compare the results of the fits with the expected values from the input distributions. In Fig. 5 we compare the results before and after the bias correction. As explained below, in the final test section, for the corrected fluxes we set the flux limit at 5 and 7 counts in the innermost region in the soft and hard band, respectively, whereas for the uncorrected fluxes we are forced to use limiting flux of 10 and 12 counts, respectively. From the results of the maximum likelihood fit it is evident that after the flux correction results are in very good agreement with the input value, whereas the distribution of the uncorrected fluxes suffers for a bias. This effect is more evident in the hard band where the background level is higher.

A possible alternative to the correction of the measured fluxes is the use of a completeness function allowing for a probability higher than unity for those fluxes where faint sources are wrongly detected. Such a probability function can be obtained by comparing the number of input and output sources in simulations as a function of their output fluxes instead of the (usually considered) input ones. In any case, this probability function will depend on the input Log N–Log S and it will be necessary to perform simulations with a number count distribution as close as possible to the unknown distribution of the sky sources (an iterative approach would be required). On top of that, the sensitivity limit of a survey adopting this procedure to correct for the Eddington bias will be a factor of  $\sim 2$  brighter than the correction of fluxes discussed above. Thus we followed the first procedure.

#### 4.4. Final tests and flux limits

In order to investigate any systematic error in our analysis we verified how the entire procedure works on different and independent simulated samples. Thus, we have generated different samples of sources with different slopes and normalizations of the integral flux distribution, comparing the input sample with the output of the detection procedure, after the correction for the flux bias and the sky coverage. Again, to assess the goodness of our analysis and to derive the flux limit, we perform a maximum likelihood fit to the differential

(unbinned) flux distributions.

In Fig. 6 we compare the input integral flux distribution (dashed line) with the output one before (dotted line) and after (solid line) the correction for the Eddington bias. As stated above, without the flux correction for this bias, a reliable flux limit is about a factor 2 larger. This happens because all the detected sources with input fluxes in the range 5–10 counts range are detected typically with 10–15 counts. As a consequence the slope of the faint tail of the distribution of uncorrected fluxes is overestimated. This effect depends on the background level and on the slope of the distribution. It is more important in the hard band where the background is higher, and where the source distribution has a larger slope. As illustrated in Fig. 6 in all cases we are able to recover the input distributions with high accuracy and with different input slopes down to 5 and 7 counts in the soft and hard band, respectively (corresponding to fluxes of  $2.4 \times 10^{-17}$  and  $2.1 \times 10^{-16}$  erg s<sup>-1</sup> cm<sup>-2</sup>). These numbers refer to the innermost regions and rising to 5, 6 and 8 counts in the other regions (7, 7 and 10 in the hard band).

## 5. Log N–Log S distribution

Within the 8' radius region in which our analysis has been carried out we detected 244 and 177 sources in the soft and hard band, respectively (Fig. 7). These sources are detected independently in the two images for a total number of 278 sources. This is at variance with e.g. Rosati et al. (2001) who made a detection over the entire 0.5–7 keV energy band and then pick up sources with signal to noise ratio larger than 2.1 in the 0.5–2 keV and 2–7 keV energy bands. Given a typical source spectrum and taking into account the different background levels in the two bands this latter approach is in general more efficient in the source detection, because it uses all the signal available, but it is not well suitable for our purposes. Infact, our final aim is drawing the flux distributions in the two bands down to the faintest limits, where the detection is highly incomplete and to do this we based on the results of the Monte Carlo simulations: if we perform the detection and the photometry in the two bands independently we can simulate all the procedures directly, whereas if we perform the detection in the full band we have to assume an input spectrum for the sources to simulate the photometry in the two bands making the evaluation of the sky coverage at the faint end tricky.

To further characterize the detected sources we computed the hardness ratio  $HR = (H - S)/(H + S)$  where  $H$  and  $S$  are the net counts in the hard and the soft band corrected for PSF and vignetting losses, respectively. There are 34 sources ( $\sim 12\%$  of the total number of detected sources) that are revealed only in the hard band ( $HR = 1$ ), and 101 sources

( $\sim 36\%$ ) that are revealed only in the soft band ( $HR = -1$ ). As can be seen in Fig. 8, there is a progressive hardening of the detected sources when plotted as a function of the soft flux indicating that the deeper we go in the soft band, the larger the number of sources responsible for the XRB at higher energies. This is particularly evident at 0.5–2 keV fluxes larger than  $\sim 10^{-15}$  erg s $^{-1}$  cm $^{-2}$  for which no source with  $HR > 0$  are observed (e.g. Tozzi et al. 2001; Brandt et al. 2001b), whereas the large number of sources at low fluxes undetected in the hard band ( $HR = -1$ ) may weaken the trend. Sources with no soft X-ray counterparts are likely candidate for type II quasar (Norman et al. 2001; Stern et al. 2001). The small number of hard sources not detected in the soft band indicate that even in highly obscured AGN a sizeable soft emission can still be produced due to, e.g., scattering, partial covering of the central radiation or from starburst emission around the AGN (e.g. Turner et al. 1997). This confirms that also at these extreme flux levels the ratio between soft and hard X-ray emission is  $\sim 1 - 10\%$ . In addition, as shown in Barger et al. (2001), the effects of obscuration get significantly reduced at  $z \sim 2$ , since we observe in the soft band the harder 1.5–6 keV rest frame interval.

In order to characterize the flux distribution of sources detected in the soft band we performed a maximum likelihood fit with a power-law distribution. We obtain as a best fit

$$N(> S) = 438 \left( \frac{S}{2 \times 10^{-15}} \right)^{-0.65} \text{ cgs.} \quad (1)$$

The error at 68% confidence level for the normalization is  $K_{15} = 438^{+82}_{-68}$  ( $K_{15}$  means that fluxes are measured in units of  $2 \times 10^{-15}$  erg s $^{-1}$  cm $^{-2}$ ), while for the slope is  $\alpha_s = 0.65 \pm 0.05$  (see also Fig. 9). This value is slightly different from the one reported in Campana et al. (2001) by less than  $1\sigma$ . This is mainly due to the improvements in the total background map calculations. Maximum likelihood analysis provide an accurate description of the errors only in the case of good fits. To assure this we adaptively binned the source distribution in order to contain 10 sources per bin. The fit of the binned data with the same power law gives a good fit by means of a  $\chi^2$  test (null hypothesis probability  $\sim 10\%$ ).

In order to test the influence of the Eddington bias correction in the fit of the slope and normalization of the Log N–Log S, we fit with the same maximum likelihood routine the uncorrected number counts. As explained above, a further implication of the Eddington bias correction is that the detection can be performed at fainter fluxes. Our soft band limiting fluxes are, in fact,  $F_{\text{lim}} = 4.9 \times 10^{-17}$  and  $F_{\text{lim}} = 2.4 \times 10^{-17}$  erg s $^{-1}$  cm $^{-2}$  before and after the correction, respectively. We find that the normalization does not change significantly ( $K_{15} = 420^{+80}_{-68}$ ) while the slope is only marginally consistent with what measured after the bias correction ( $\alpha_s = 0.72 \pm 0.05$ ; see also Fig. 9).

Our bias corrected normalization and slope, are in good agreement with earlier results

obtained with ROSAT (Hasinger et al. 1998), Chandra (Tozzi et al. 2001) and XMM-Newton (Hasinger et al. 2001; Baldi et al. 2001) up to their faintest flux levels ( $> 10^{-16}$  erg s $^{-1}$  cm $^{-2}$ ).

The total extragalactic background in the soft band is usually evaluated in the 1–2 keV band to limit contribution from our Galaxy. The absolute value of the XRB is still a matter of debate. The 1–2 keV XRB estimates are clustered around two different values: Hasinger et al. (1993) and Gendreau et al. (1995) obtained a value of  $3.76 \times 10^{-12}$  erg s $^{-1}$  cm $^{-2}$  deg $^{-2}$ . This is in contrast with the estimate derived by Chen et al. (1997; see also Hasinger 1996) based on a joint ROSAT/ASCA fit yielding a flux of  $4.42 \times 10^{-12}$  erg s $^{-1}$  cm $^{-2}$  deg $^{-2}$  (i.e.  $\sim 20\%$  higher). An intermediate value has recently been obtained by Kuntz, Snowden & Mushotzky (2001) using ROSAT PSPC observations with  $3.99 \times 10^{-12}$  erg s $^{-1}$  cm $^{-2}$  deg $^{-2}$  and Garmire et al. (2002, in preparation) using Chandra  $4.19 \times 10^{-12}$  erg s $^{-1}$  cm $^{-2}$  deg $^{-2}$ . Based on our Log N–Log S distribution we can resolve in point sources a flux of  $5.58 \times 10^{-13}$  erg s $^{-1}$  cm $^{-2}$  deg $^{-2}$  for sources fainter than  $10^{-15}$  erg s $^{-1}$  cm $^{-2}$ . Summing to this the contribution from the Lockman hole (Hasinger et al. 1998) we obtain a resolved flux of  $3.57 \times 10^{-12}$  erg s $^{-1}$  cm $^{-2}$  deg $^{-2}$ . As pointed out by Rosati et al. (2001) we have also to include the contribution from cluster of galaxies recognized to be at a level of 6% in the 1–2 keV energy band (Rosati et al. 1998). In conclusion, in the case of the lower background estimate we are able to fully resolve it as arising from point sources, taking the higher value we can resolve 87%.

The slope of the faint end counts converges slower than logarithmically and therefore the faint sources have a very small contribution to the XRB. Extending to lower fluxes the source distribution we can add just a 4% more. This may leave space for a  $\lesssim 9\%$  truly diffuse emission produced by the warm/hot diffuse intergalactic medium which is estimated to contribute at a 5–15% level (Phillips et al. 2001).

A final caveat concerns the total flux of the point sources which suffers from several uncertainties: source flux conversion, variation of the power law index from source to source, cosmic variance (the CDFS is depleted of bright sources), Log N–Log S power law index and normalization uncertainties. We estimate an error at a level of 7%.

In the case of the hard band, a fit with a single power-law source distribution does not provide a good description of the data (binning the data as before, we obtain a probability of the null hypothesis  $\sim 0.02\%$ ). Moreover due to the lack of bright sources in the CDFS, our data cannot be matched directly with earlier result. So we normalized the distribution of our 177 sources, see Fig. 9) to the ASCA data (della Ceca et al. 2000). The limiting flux is  $2.1 \times 10^{-16}$  erg s $^{-1}$  cm $^{-2}$  and raises to  $F_{\text{lim}} = 3.7 \times 10^{-16}$  erg s $^{-1}$  cm $^{-2}$  if the Eddington bias correction is not applied.

Thus, we turn to a smoothly joined power–law model:

$$N(> S) = 1.2 \times 10^4 \left[ \frac{(2 \times 10^{-15})^{\alpha_{h1}}}{S^{\alpha_{h1}} + S_0^{\alpha_{h1} - \alpha_{h2}} S^{\alpha_{h2}}} \right] \text{cgs}, \quad (2)$$

fixing the bright flux slope and the normalization to the ASCA value, i.e.  $\alpha_{h1} = 1.67$  (della Ceca et al. 2000). The faint end slope and the break flux  $S_0$  are fitted to the data. The maximum likelihood fit yields  $\alpha_{h2} = 0.49 \pm 0.05$  and  $S_0 = 9.6_{-1.0}^{+1.2} \times 10^{-15} \text{ erg s}^{-1} \text{ cm}^{-2}$  (all at 68% confidence level for a single parameter; see Fig. 9). Without correcting for the Eddington bias, the break flux slightly changes  $S_0 = 10.5_{-1.0}^{+1.2} \times 10^{-15}$  and the fitted slope is  $\alpha_{h2} = 0.56 \pm 0.05$ . The slope value is slightly flatter (within  $1\sigma$ ) than what found in Campana et al. (2001).

The problem of estimating the background level in the hard 2–10 keV band is even more serious than in the soft band. Also in this case different estimates exist but the range of variation is as high as 50%. The limiting values are on the lower side the ones from UHURU and HEAO-1  $1.6 \times 10^{-11} \text{ erg s}^{-1} \text{ cm}^{-2} \text{ deg}^{-2}$  (Marshall et al. 1980; see also Ueda et al. 1999 based on ASCA) and on the higher side the (more recent) ones from BeppoSAX and ASCA  $2.4 \times 10^{-11} \text{ erg s}^{-1} \text{ cm}^{-2} \text{ deg}^{-2}$  (Chiappetti et al. 1998; Vecchi et al. 1999; Ishisaki et al. 2000; Perri & Giommi 2000), in agreement with the old Wisconsin measurements (McCammon et al. 1983).

With our number counts distribution, we are able to account for  $1.99 \times 10^{-11} \text{ erg s}^{-1} \text{ cm}^{-2} \text{ deg}^{-2}$ . This value is higher than the UHURU and HEAO-1 estimate by 24% likely ruling out it. With respect to the higher 2–10 keV background estimate our source distribution can account for 83% of the background resolved in point sources. Also in this case the faint end tail converges slower than logarithmically and we can comprise up to 87% of the hard background (see also Campana et al. 2001). A new population of sources, possibly contributing also at higher energies, is therefore needed if one wants to fully resolve the background into point sources.

In this case, the error on the background flux resolved into sources is dominated by the uncertainty in the flux conversion factor, resulting in a 10% error.

## 6. Conclusions

Based on the experience developed in the ROSAT HRI data analysis (Lazzati et al. 1999; Campana et al. 1999) we build up a procedure for the automatic detection and characterization of sources in Chandra ACIS fields. The main difference between our wavelet

algorithm (BMW-Chandra) and the standard CIAO `wavdetect` (Freeman et al. 2001) is the use of the multi-resolution technique. As explained, this makes the BMW-Chandra algorithm less flexible but faster and therefore more suitable for the analysis of large data sets and for Monte Carlo tests. The Chandra deep fields are, of course, the most intriguing fields to probe the algorithm. Here we have described the procedures we used to simulate and analyze in details the CDFS. The simulations we performed allow us to safely conclude that our detection procedures are robust in terms of number of spurious sources, positional accuracy, flux estimate down to the quoted limits. In this respect the Eddington bias correction is especially important, allowing us to approach the theoretical detection limit of 3 photons (Damiani et al. 1997b).

Scientific results have been previously discussed in Campana et al. (2001), here we improve and complement them. We independently detect 244 and 177 sources in the soft and hard band, respectively for a total number of 278 sources. Source distributions can be safely recovered down to fluxes  $2.4 \times 10^{-17}$  and  $2.1 \times 10^{-16}$  erg s $^{-1}$  cm $^{-2}$  in the soft and hard energy band, respectively. These are a factor of  $\gtrsim 2$  deeper than current estimates. Note that being still in the photon detection limit, an improvement by a factor of  $\sim 2$  in the Log N–Log S reconstruction corresponds to an effective doubling of the observing time.

There is general consensus that the main constituents of the soft 1–2 keV XRB can be ascribed to broad line AGN (i.e. Seyfert 1 galaxies; Hasinger et al. 1998; Schmidt et al. 1998). At faint fluxes ( $\lesssim 10^{-15}$  erg s $^{-1}$  cm $^{-2}$ ) nearby ( $z \lesssim 0.6$ ) optically-normal (possibly low luminosity AGN) galaxies are also being detected as soft sources (Fiore et al. 2000; Barger et al. 2001; Tozzi et al. 2001; Brandt et al. 2001a; Schreier et al. 2001; Koekemoer et al. 2001). Our analysis of the CDFS extends the source flux distribution down the faintest level of  $2.4 \times 10^{-17}$  erg s $^{-1}$  cm $^{-2}$ . We found that even at these low fluxes the Log N–Log S distribution can still be represented by the extrapolation from higher fluxes without upward trends. Including the contribution from cluster of galaxies (Rosati et al. 1998), we are able to resolve in point sources  $> 90\%$  of the soft XRB, the exact value depending on the sky level itself. Our results are also in agreement with the recent fluctuation analysis on the HDFN down to  $7 \times 10^{-18}$  erg s $^{-1}$  cm $^{-2}$  (Miyaji & Griffiths 2002).

In the hard band the XRB is made by the superposition of absorbed and unabsorbed sources (Setti & Woltjer 1989). The steeper power law index observed in bright AGN implies that a population of faint hard sources is present, likely affected by a considerable absorption. Studies with Chandra and XMM-Newton are now discovering these sources identifiable with Type II AGN unrelated to the morphological type (Schreier et al. 2001; Koekemoer et al. 2001). We note that only a small fraction of hard source are not detected in the soft band, likely indicating that at least 1 – 10% of the flux is in any case emitted in the soft band.

Our analysis lead to the extension of the Log N–Log S source flux distribution down to  $2.1 \times 10^{-16}$  erg s $^{-1}$  cm $^{-2}$ . At this level we can rule out the UHURU/HEAO-1 estimate and account for 87% of the BeppoSAX/ASCA estimate. The fluctuation analysis by Miyaji & Griffiths (2002) does not add much stopping at  $1 \times 10^{-16}$  erg s $^{-1}$  cm $^{-2}$  but with a large error.

The analyzed field of view is small and cosmic variance likely plays a role. We plan to carry out the same analysis of the Chandra HDFN in order to confirm the present results and to perform a joint analysis with other shallower and more extended surveys in order to cover with good statistics the bright flux ends (Moretti et al., in preparation).

Chandra with its superb angular resolution opens the possibility to extend at even lower fluxes the source distribution. In fact, at the present level sources are still photon limited. This will allow to deepen our knowledge of the distant universe, allowing to probe the accretion power over the history of the X–ray universe, and its implications for structure formation and the epoch of reionization.

We thank the continuous support of the Chandra Help Desk and the CIAO team for the organization of Chandra/CIAO workshop. We also thank M. Markevitch and the anonymous referee for their suggestions. This work was supported through CNAA, Co-fin, ASI grants and Funds for Young Researchers of the Università degli studi di Milano.

## REFERENCES

Baganoff, F. K. 1999, ACIS Memo 162,  
[http://asc.harvard.edu/cal/Links/Acis/acis/Cal\\_prods/bkgrnd/current/index.html](http://asc.harvard.edu/cal/Links/Acis/acis/Cal_prods/bkgrnd/current/index.html).

Baldi, A., Molendi, S., Comastri, A., Fiore, F., Matt, G., Vignali, C. 2001, ApJ in press  
(astro-ph/0108514)

Barger, A. J., Cowie, L. L., Mushotzky, R. F., Richards, E. A. 2001, AJ, 121, 662

Bautz, M., et al. 1998, SPIE, 3444, 210

Brandt, W. N., et al. 2001a, AJ, 122, 1

Brandt, W. N., et al. 2001b, AJ, in press (astro-ph/0108404)

Bijaoui A., Giudicelli, M. 1991, Exp Astron., 1, 347

Campana, S., et al. 1999, ApJ, 524, 423

Campana, S., Moretti, A., Lazzati, D., Tagliaferri, G. 2001, ApJ 560 L19

Chiappetti, L., Cusumano, G., del Sordo, S., Maccarone, M.C., Mineo, T., & Molendi, S. 1998, in *The Active X-ray Sky: Results from BeppoSAX and RXTE*. eds. L. Scarsi, H. Bradt, P. Giommi, & F. Fiore. (Elsevier, Amsterdam), 610

Damiani, F., Maggio, A., Micela, G., Sciortino, S. 1997a, ApJ, 483, 350

Damiani, F., Maggio, A., Micela, G., Sciortino, S. 1997b, ApJ, 483, 370

della Ceca, R., Braito, V., Cagnoni, I., Maccacaro, T. 2000, Proceedings of the Conference SAIt 2000, Mem. SAIt in press

Fiore, F., et al. 2000, New Astr., 5, 143

Freeman, P. E., et al. 2001, ApJ, in press (astro-ph/0108429)

Garmire, G. P., et al. 2002, ApJ submitted

Gendreau, K.C., et al. 1995, PASJ, 47, L5

Giacconi, R., et al. 2001, ApJ, 551, 624

Grebenev, S. A., Forman, W., Jones, C., Murray, S. 1995, ApJ, 445, 607

Hasinger, G., et al. 1993, A&A, 275, 1

Hasinger, G., et al. 1998, A&A, 329, 482

Hasinger, G., et al. 2001, A&A, 365, L45

Hornschemeier, A. E., et al. 2000, ApJ, 541, 49

Koekemoer, A. N., et al. 2001, ApJ in press (astro-ph/0110385)

Kuntz, K. D., Snowden S. L., Mushotzky R. F. 2001, ApJ, 548, L119

Ishisaki, Y., et al. 2000, in *Broad Band X-ray Spectra of Cosmic Sources – COSPAR* , eds. K. Makishima, L. Piro, & T. Takahashi (Pergamon Press)

Lazzati, D., Campana, S., Rosati, P., Chincarini, G., Giacconi, R. 1998, A&A, 331, 41

Lazzati, D., et al. 1999, ApJ, 524, 414

Marshall, F. E., et al. 1980, ApJ, 235, 4

McCammon, D., Burrows, D. N., Sanders, W. T., Kraushaar, W. L. 1983, *ApJ*, 269, 107

Miyaji, T., Griffiths, R. E. 2002, *ApJ* in press (astro-ph/0111393)

Mushotzky, R. F., Cowie, L. L., Barger, A. J., Arnaud, K. A. 2000, *Nat*, 404, 459

Norman, C., et al. 2001, *ApJ*, in press (astro-ph/0103198)

Panzera, M. R., et al. 2002, to be submitted to *A&A*

Perri, M., Giommi, P. 2000, *A&A*, 362, L57

Pislar, V., Durret, F., Gerbal, D., Lima Neto, G. B., Slezak, E. 1997, *A&A*, 322, 53

Phillips, L. A., Ostriker, J. P., Cen, R. 2001, *ApJ*, 554, L9

Rosati, P., della Ceca, R., Burg, R., Norman, C., Giacconi, R. 1995, *ApJ*, 445, L11

Rosati, P., della Ceca, R., Norman, C., Giacconi, R. 1998, *ApJ*, 492, L21

Rosati, P., et al. 2001, *ApJ* in press

Schreier, E. J., et al. 2001, *ApJ*, 560, 127

Schmidt, M., et al. 1998, *A&A*, 329, 495

Setti, G., Woltjer, L. 1989, *A&A*, 224, L21

Slezak, E., Durret, F., Gerbal, D. 1994, *AJ*, 108, 1996

Stern, D., et al. 2001, *ApJ* in press (astro-ph/0111513)

Tozzi, P., et al. 2001, *ApJ*, 562, 42

Ueda, Y., et al. 1999, *ApJ*, 518, 656

Vecchi, A., Molendi, S., Guainazzi, M., Fiore, F., Parmar, A. N. 1999, *A&A*, 349, L73

Vikhlinin, A., Forman, W., Jones, C., Murray, S. 1995, *ApJ* 451, 542

Vikhlinin, A., McNamara, B. R., Forman, W., Jones, C., Quintana, H., Hornstrup, A. 1998, *ApJ*, 502, 558

Weisskopf, M. C., Tananbaum, H. D., Van Speybroeck, L. P., O'Dell, S. L. 2000, *SPIE*, 4012, 2

Table 1: Main characteristics of the 11 single exposures.

ID	R.A. (J2000)	Dec. (J2000)	Roll Angle	Soft.Exp. (ks)	Hard.Exp. (ks)	Nom.Expos. (ks)	$\Delta\alpha$ (pixel)	$\Delta\delta$ (pixel)	$\sigma_{\Delta\alpha}$ (pixel)	$\sigma_{\Delta\delta}$ (pixel)
0581	53.122	−27.806	47.28	15.594	15.311	18.713	0.0	0.0	0.00	0.00
0441	53.111	−27.804	166.73	55.967	54.967	55.967	72.8	7.6	0.51	0.65
0582	53.111	−27.804	162.92	130.486	128.595	130.486	70.9	8.6	0.77	0.65
1431	53.122	−27.806	47.28	110.105	107.560	123.008	1.2	−0.7	0.64	0.61
1672	53.120	−27.813	326.90	95.138	95.138	95.138	20.2	−51.1	0.79	0.86
2239	53.117	−27.811	319.20	123.999	129.732	130.738	38.9	−39.7	0.77	0.81
2312	53.118	−27.811	329.91	123.686	123.686	123.686	31.2	−35.4	0.63	0.72
2313	53.117	−27.811	319.20	130.389	130.389	130.389	37.7	−39.0	0.62	0.59
2405	53.120	−27.812	331.80	58.215	55.725	59.635	16.4	−50.1	0.70	0.67
2406	53.118	−27.810	332.18	29.686	28.696	29.686	30.7	−34.3	0.91	0.59
2409	53.117	−27.811	319.20	68.982	68.982	68.982	38.8	−39.1	0.92	1.02

Pixels are at nominal rebin (i.e. 0.49'').

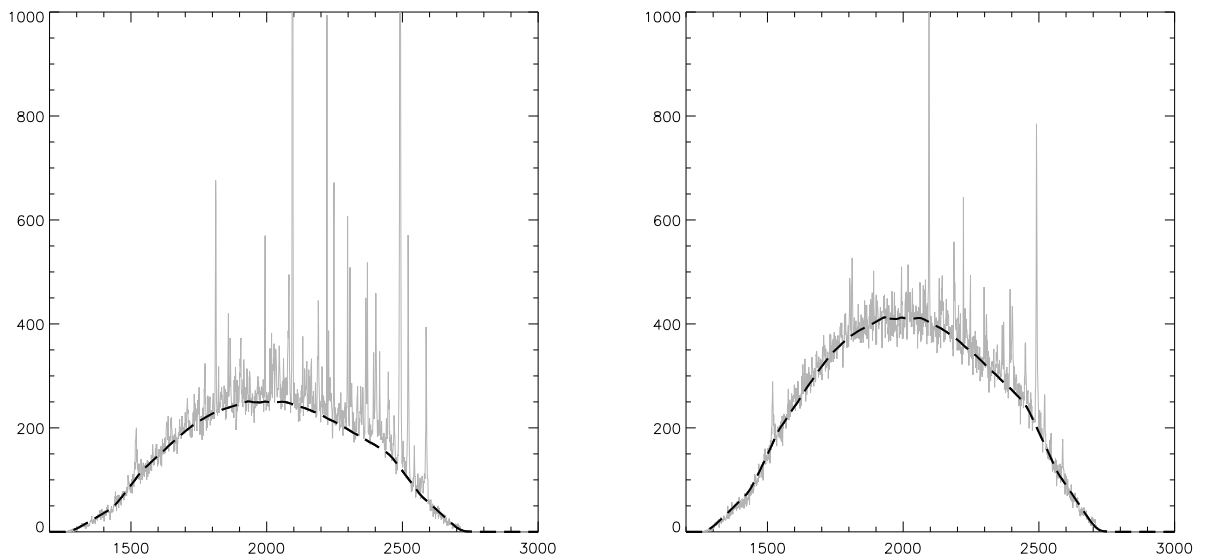


Fig. 1.— The comparison between the total background maps and the real data in the soft band (left panel) and hard band (right panel). We compare the projections of the columns of the accumulated images (grey solid line) with the projection of the total background map (black dashed line). On the X axis the units are rebinned pixels and on the Y axis are simply the counts.

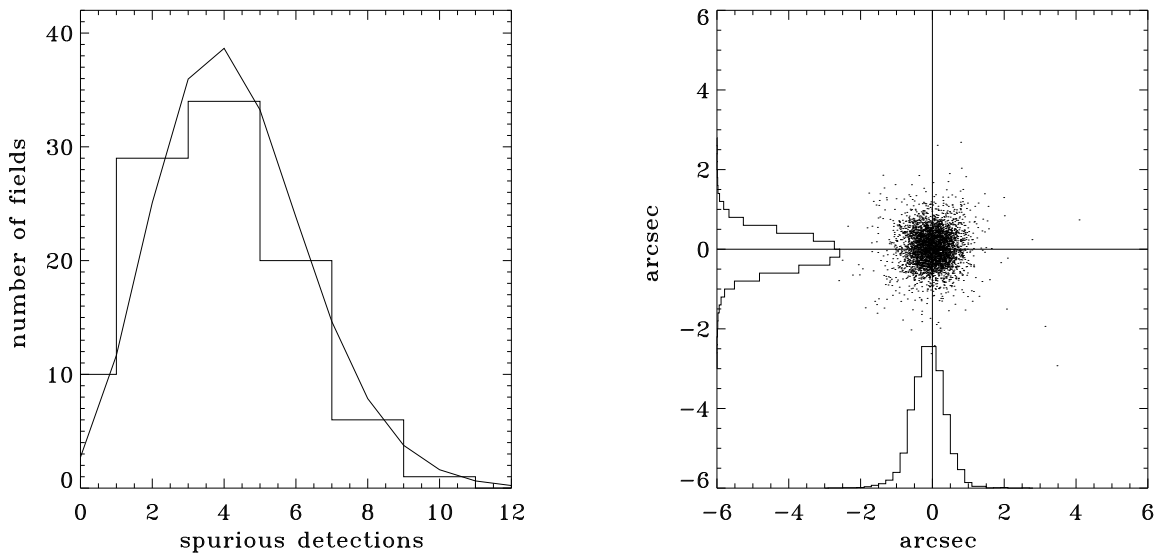


Fig. 2.— The performance of the BMW detection algorithm. In the left panel, the distribution of the of number of spurious detections in the simulated fields is plotted and compared with the expected Poissonian distribution with a mean value of 4.3. In the right panel we plot the differences between the input position of the simulated sources across the  $8'$  radius field of view and the position recovered by the detection algorithm. The difference distributions are very well approximated by Gaussians centered in zero and with a standard deviation of 0.6 arcsec.

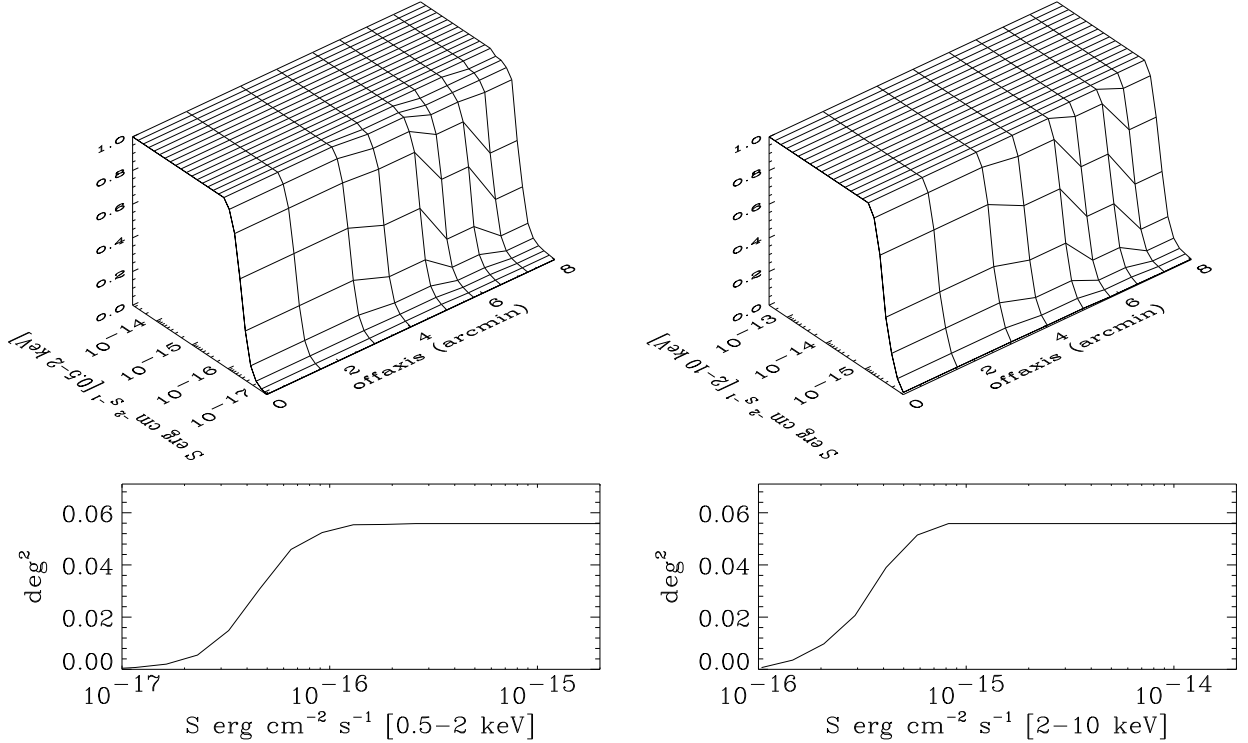


Fig. 3.— In the upper part of the figure the graphics of the probability of detecting a source (completeness function) in the soft and hard bands are shown. They are functions of the flux of the sources and due to the combination of the PSF broadening and the vignetting they are also functions of the distance from the center of the image (i.e. the off-axis angle). We have divided the CDFS in 4 circular coronae and calculated 4 different completeness functions to take into account this effect. In the lower panels the total sky coverages in the soft and hard band in unit of square degrees are plotted: they are calculated as the sum of the contributions from the 4 different circular coronae.

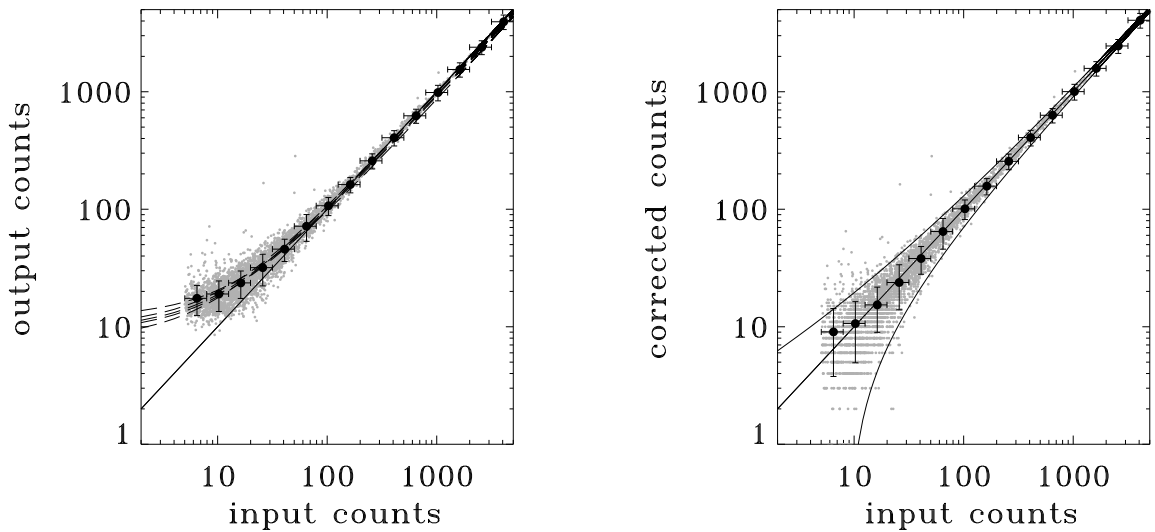


Fig. 4.— In the left panel the measured counts versus input simulated counts in the soft band are plotted (little grey dots). It is evident that the detection limit is about 10 counts and where the detection is incomplete (below 30 counts) the measured counts are overestimated. The dashed lines show the analytical approximation of the Eddington bias in the measure of faint fluxes for different off-axis angles. The solid line is the straight lines  $y = x$ . The black big dots are the mean values of the output counts for different bins of input counts. The right panel shows the counts corrected by the inverse of the analytical function (little grey dots). The black big dots are the mean values of the corrected counts for different bins of input counts. Overplotted with the the solid lines are the straight lines  $y = x$  and the 90% expected Poisson uncertainties.

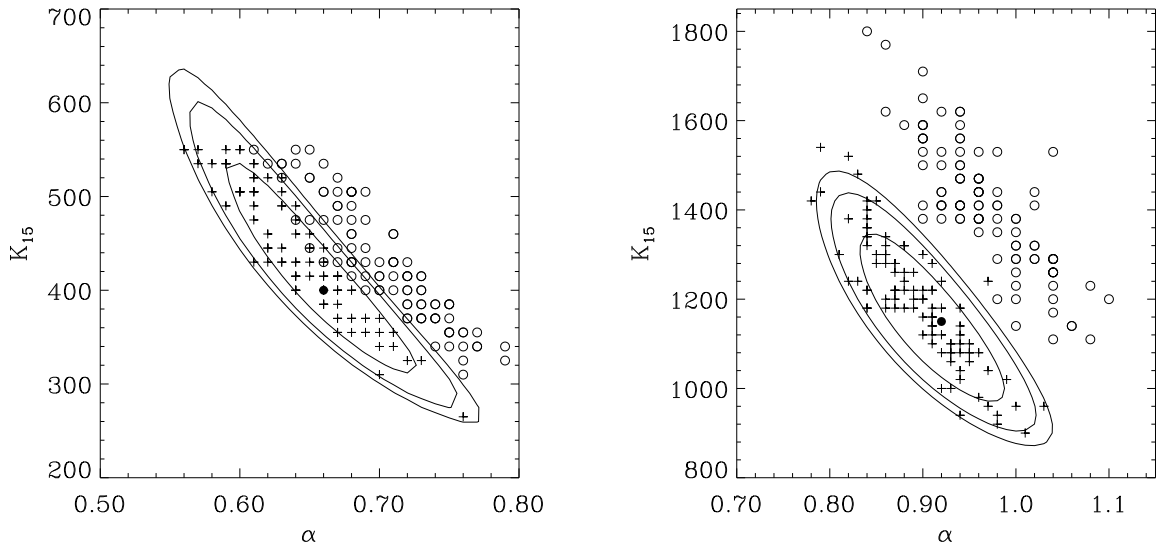


Fig. 5.— Left panel: values of the normalization  $K_{15}$  (in units of  $2 \times 10^{-15}$  erg s $^{-1}$  cm $^{-2}$ ) and the slope  $\alpha$  of the source integral distribution as obtained for each of 100 simulated fields. Simulations are carried in the soft 0.5–2 keV energy band. Crosses refer to fits with the Eddington bias correction, whereas open circles to fits on uncorrected data. The central filled dot indicate the input values ( $K_{15} = 400$ ;  $\alpha = 0.66$ ). The 68%, 90% and 99% confidence level are overplotted. Right panel: same as in the left panel but for the hard 2–10 keV energy band. Input values are  $K_{15} = 1150$ ;  $\alpha = 0.92$ .

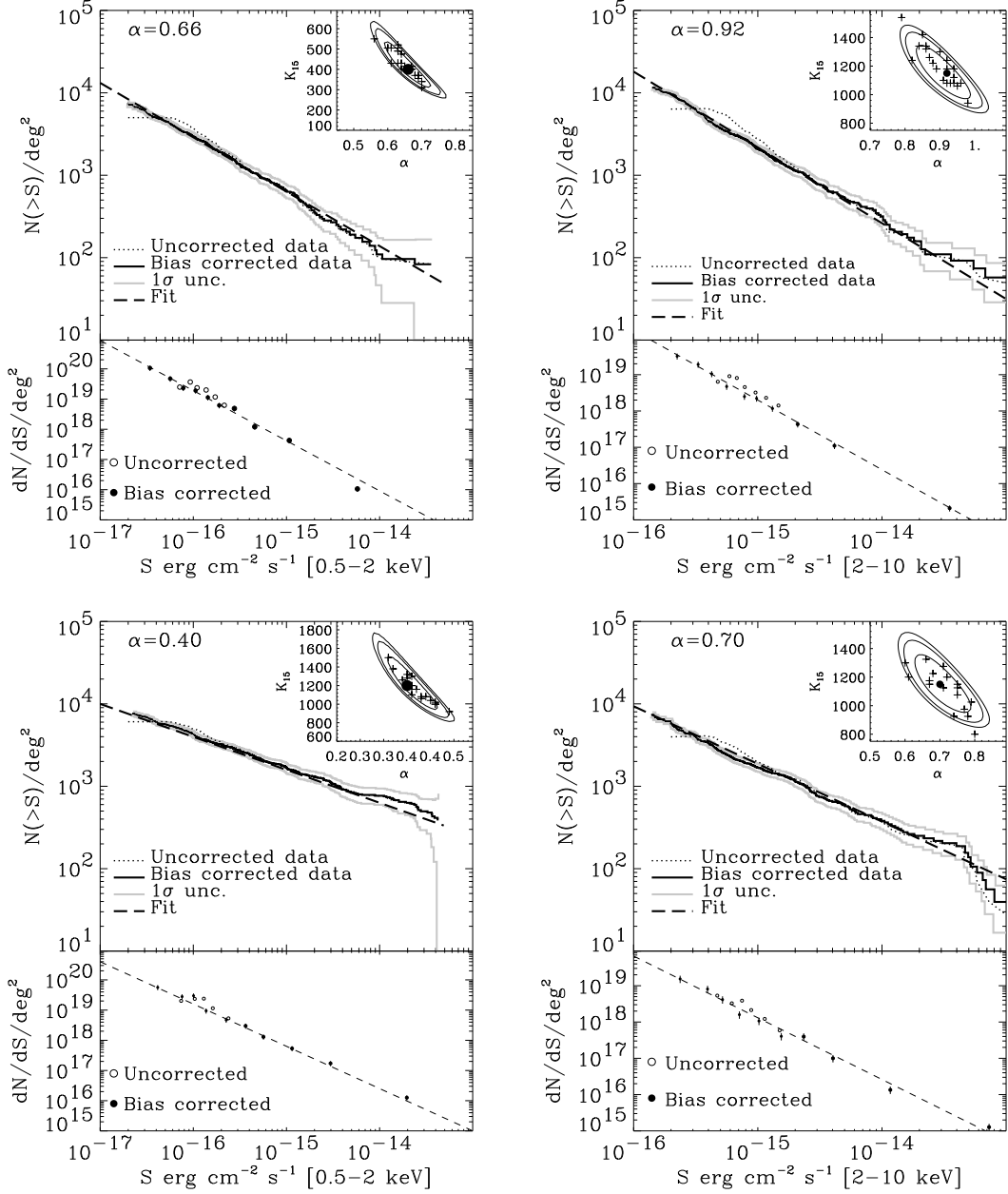


Fig. 6.— We report the results of four sets of simulations, two in the soft and two in the hard band. Each set has different slope and normalization of input fluxes and consists of about 15 fields. In each field about 300 sources are present. In the main upper panels we report the results relative to one field for each set: we compare the input integral distribution (dashed line) with the one recovered after the detection (dotted line) and after the bias correction (solid line). In the inserts we plot the results from the maximum likelihood fits relative to every field of the set (crosses) and the expected value (black dot). In addition we overplot the uncertainties (68%, 90%, 99% confidence level). In the lower panels the differential distributions are plotted: the data have been adaptively smoothed to have the same number of sources per bin.

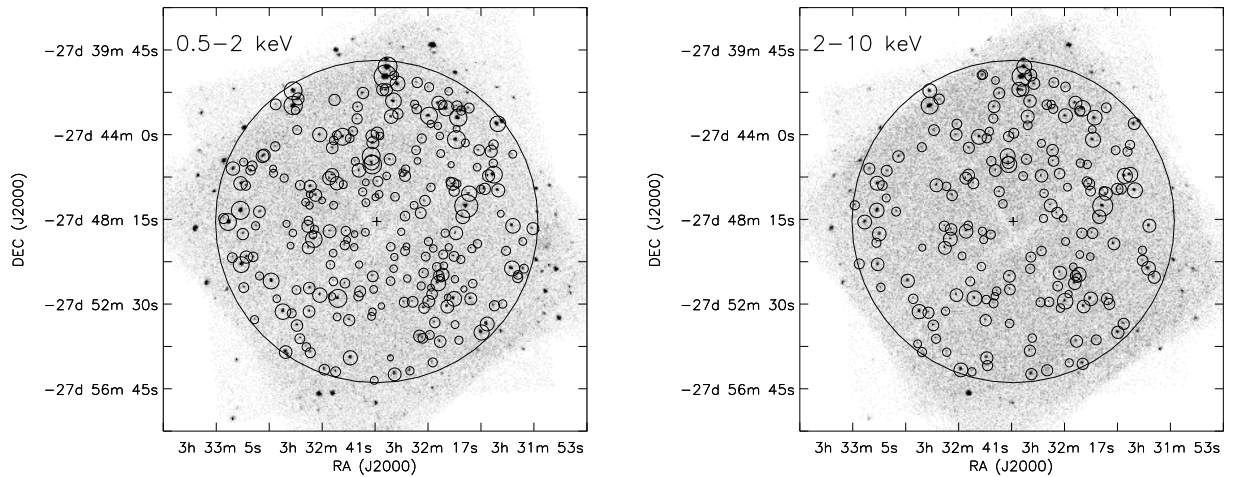


Fig. 7.— The detected sources in the soft band (left) and in the hard band (right). The dimensions of the circles are proportional to the logarithm of the estimated flux. We restricted our analysis to the central 8 arcmin radius circle, assuming as center the aim point of the observation ID581.

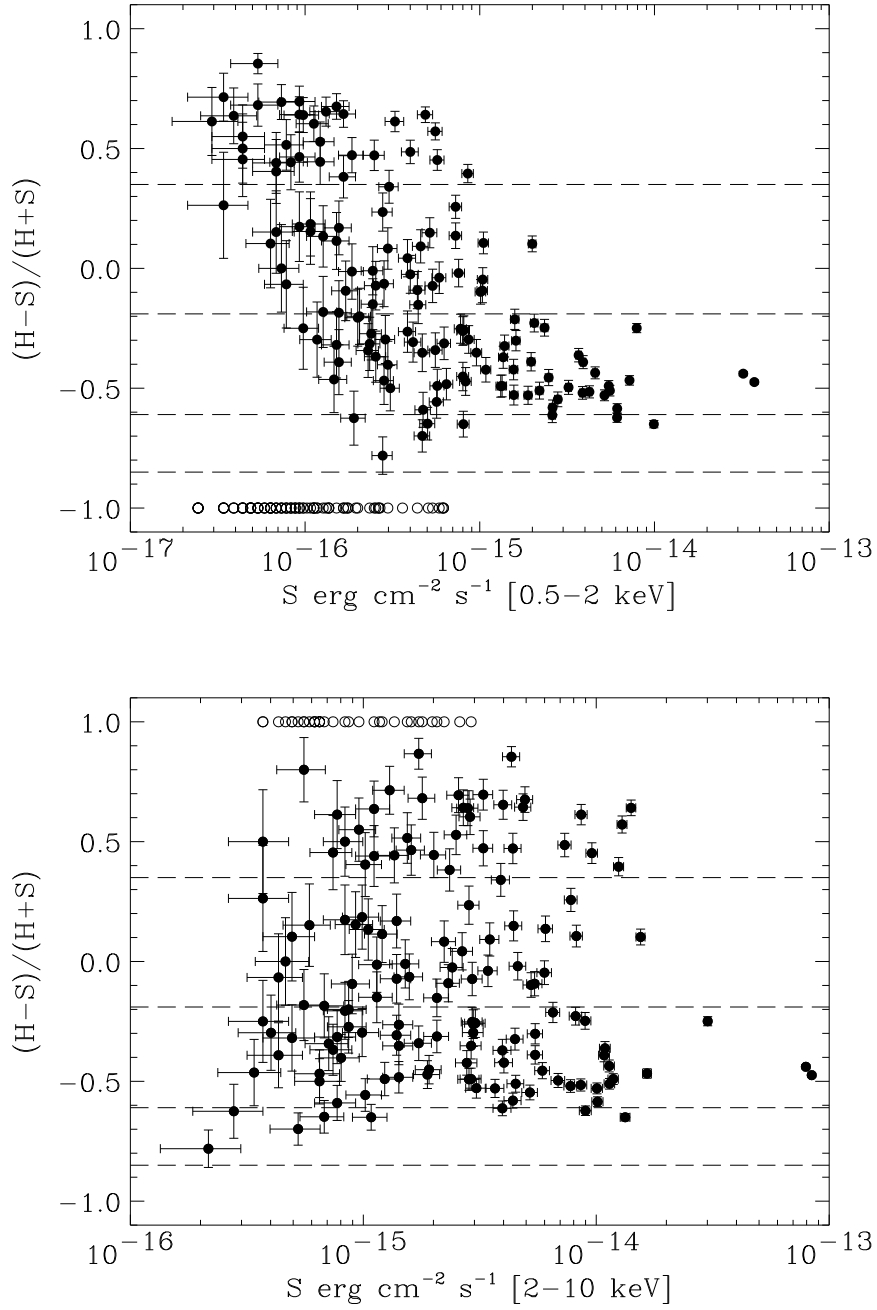


Fig. 8.— Color diagram of the detected sources versus the soft flux (upper panel) and hard flux (lower panel). Sources undetected in the hard and soft band are marked with open circle with a color of  $-1$  and  $1$ , respectively. Dashed lines refer to hardness ratio of power law models with photon index  $3$ ,  $2$ ,  $1$  and  $0$  (from bottom to top), respectively.

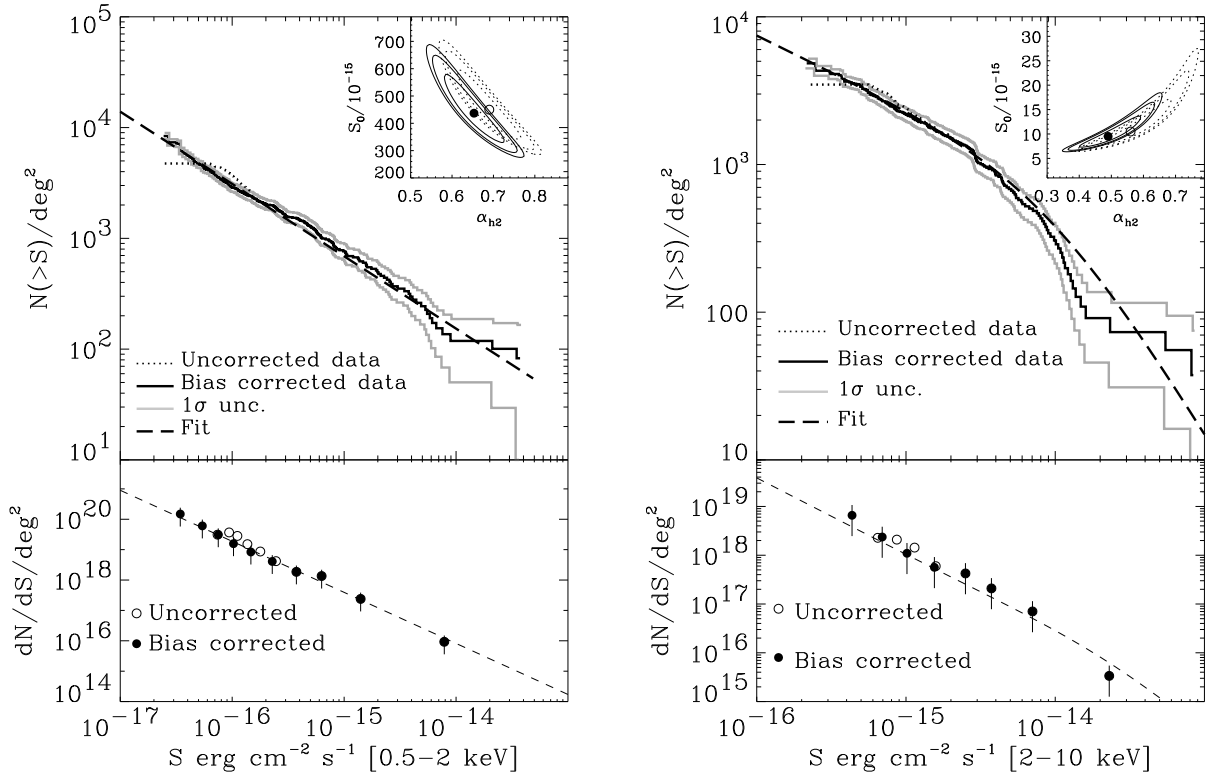


Fig. 9.— Left panel: Soft band Log N–Log S from inner 8' radius of the 1 Ms observation of the CDFs (thick solid line) in the range  $2 \times 10^{-17} - 3 \times 10^{-14}$  erg s $^{-1}$  cm $^{-2}$  for an average  $\Gamma = 1.4$  power–law spectrum. The gray thick line shows the 1 $\sigma$  confidence region taking into account the number statistics and the flux conversion uncertainties. The thick dashed solid line shows the best maximum likelihood fit. The dotted line represents the Log N–Log S distribution *without* the correction for the Eddington bias. In the insert we plot the best value and the uncertainties for the corrected fluxes (filled circle and continuous line) and the uncorrected ones (empty circle and dashed lines).

Right panel: Hard band Log N–Log S from inner 8' radius of the 1 Ms observation of the CDFs (thick solid line) in the range  $2 \times 10^{-16} - 2 \times 10^{-14}$  erg s $^{-1}$  cm $^{-2}$ . Lines are as in the right panel. In the lower panels the differential distribution of corrected fluxes (filled circles) and uncorrected fluxes (open circles) are plotted with the fit. The data have been adaptively binned to have the same number of sources per bin